Article
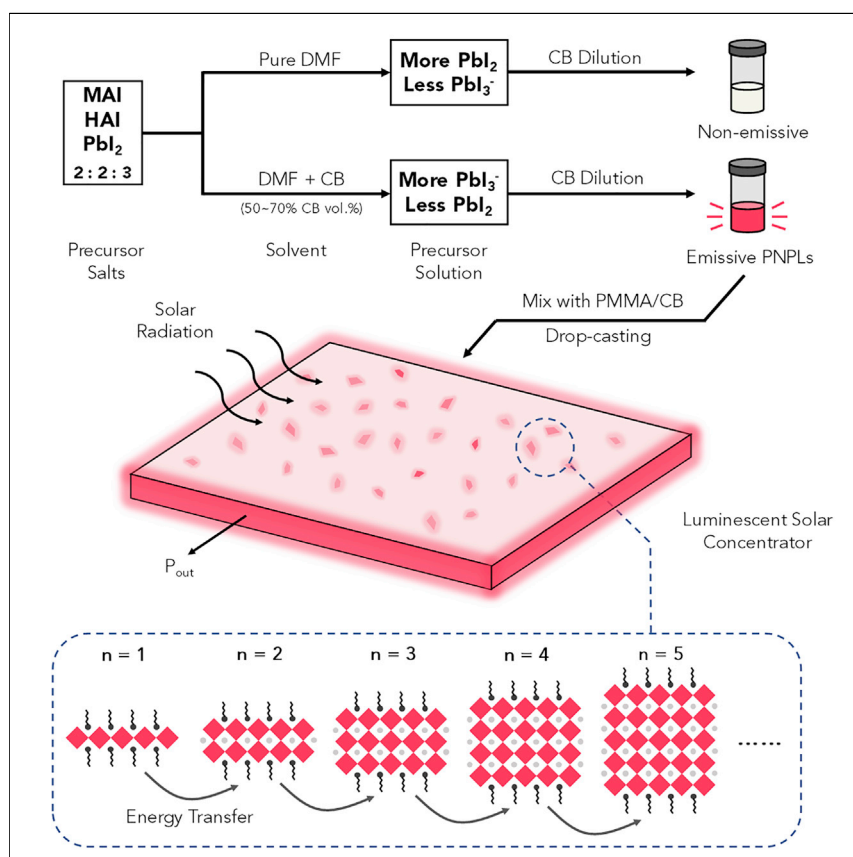
Solvent-Solute Coordination Engineering for Efficient Perovskite Luminescent Solar Concentrators

Ziliang Li, Andrew Johnston, Mingyang Wei, ..., Yuan Liu, Osman M. Bakr, Edward H. Sargent

ted.sargent@utoronto.ca

HIGHLIGHTS

Solvent-Pb^{2+} coordination engineering enables tailoring of the MQW distribution

56% PLQY for PNPL-PMMA films

2.0% optical conversion efficiency for 10 × 10 cm PNPL-based LSCs

By judiciously engineering solvent and anti-solvent ratios during the preparation of precursors, Li et al. exploit solvent-Pb^{2+} coordination to control the multiple quantum well (MQW) distribution in perovskite nanoplatelets (PNPLs). They report 10 × 10 cm luminescent solar concentrator (LSC) devices based on PNPL/poly(methyl methacrylate) composites; these reach an optical conversion efficiency of 2.0%.

Joule

CellPress

Article

Solvent-Solute Coordination Engineering for Efficient Perovskite Luminescent Solar Concentrators

Ziliang Li,[1] Andrew Johnston,[1] Mingyang Wei,[1] Makhsud I. Saidaminov,[1,3] Joao Martins de Pina,[1] Xiaopeng Zheng,[2] Jiakai Liu,[2] Yuan Liu,[1] Osman M. Bakr,[2] and Edward H. Sargent[1,4,*]

SUMMARY

Luminescent solar concentrators (LSCs) enable large-area collection of sunlight relevant to building-integrated photovoltaics. Reduced-dimensional metal halide perovskite nanoplatelets (PNPLs) have recently emerged as candidates for low-loss large-area LSCs due to the optoelectronic properties of perovskites combined with the large Stokes shift attainable using the multiple quantum well (MQW) structure. LSCs using bromine-based PNPLs have been demonstrated; however, the band gaps of bromine-based perovskites limit the absorption range. Iodine-based PNPLs allow broader absorption, but emission can be achieved only if the chemistry of PbI_x^{2-x} precursor complexes is engineered to provide the appropriate MQW distribution. Here, by controlling the polarity and Lewis basicity of the precursor solution, we modify the solvent-Pb^{2+} coordination and synthesize PNPLs having a uniform MQW distribution. This improves energy funneling, enabling a film PLQY (photoluminescence quantum yield) of 56% and 10 × 10 cm LSCs with an optical conversion efficiency of 2.0%, a 1.3-fold enhancement compared to the best previously reported room-temperature-fabricated perovskite LSCs.

INTRODUCTION

Luminescent solar concentrators (LSCs) concentrate sunlight incident from a large area to a smaller one, reducing thereby photovoltaic (PV) materials consumption. An LSC is a semi-transparent optical slab in which luminescent chromophores are embedded in a transparent waveguide. Chromophores absorb the incident photons—ideally across a broad energetic spectrum—and reemit photons at a longer wavelength. The reemitted photons are then wave guided to the edges of the LSC, where solar cells convert the now-concentrated light into electrical power.

Different chromophores have been investigated for LSC applications, including quantum dots (QDs),[1–8] organic dyes,[9–13] and rare-earth ions and their organic complexes.[14–17] The Stokes shift—the difference between the absorption onset and the emission wavelength—of these chromophores is intentionally engineered to be large to ensure that reabsorption during waveguide propagation is minimized. Recently, metal halide perovskites have emerged as candidates for LSC chromophores[18–24] due to their spectral tunability and the ease with which they can be solution processed. In particular, reduced-dimensional perovskites are suited for use in LSCs since the energy funneling provided by multiple quantum wells (MQWs)[25] results in a large Stokes shift and efficient photoluminescence (PL). A room-temperature synthesis of colloidal reduced-dimensional perovskite nanoplatelets (PNPLs)

Context & Scale

Luminescent solar concentrators (LSCs) concentrate sunlight incident from a large area to a smaller one, thereby reducing photovoltaic (PV) materials consumption and enabling building-integrated PV. Reduced-dimensional metal halide perovskite nanoplatelets (PNPLs) have recently emerged as candidates for low-loss large-area LSCs, since they combine the optoelectronic properties of perovskite materials with reduced absorption-luminescence spectral overlap. Prior LSC studies based on PNPLs used bromine-based perovskites, and their absorption spectral range was limited to wavelengths shorter than 520 nm. We engineered the precursor chemistry of iodine-based perovskites to realize a room-temperature synthesis of PNPLs that exhibit a substantially uniform distribution of quantum wells. The high photoluminescence quantum yield led to an optical conversion efficiency that is 1.3× higher than in the best previously reported room-temperature-fabricated perovskite LSCs.

Joule

CellPress

has been applied to LSC fabrication, achieving a maximum optical quantum efficiency (OQE) of 26%;[19] however, the OQE only accounts for the ratio of the number of photons emitted from the LSC edges to the total number of *absorbed* photons, irrespective of the number of photons incident on the optical slab. The absorption range of bromine-based PNPLs used in previous work is limited, resulting in an optical conversion efficiency η_{opt} (the ratio of the output power from the edges of LSCs and the input power on the top surface of the LSC) of 1.5%. There is thus significant interest in developing iodine-based PNPLs to capture more of the broad solar spectrum.

In contrast with the case of bromine-based perovskites, iodine-based perovskites require that special attention be paid to the chemistry of the precursor solution: several iodoplumbate complex species (PbI_x^{2-x}, where x = 2–6) form in the solution,[26] and these significantly impact the properties of the final perovskites.[27–32] To date, research on iodoplumbate species in perovskite precursor solutions has focused on bulk 3D perovskite thin films. These important insights have yet to be deployed in nanocrystal synthesis.

Here, we report a room-temperature colloidal synthesis of iodine-based perovskite NPLs that enables low-loss and efficient LSCs. By combining solvent and anti-solvent in different ratios during preparation of the precursor solution, we engineer the solvent-Pb^{2+} coordination to control the MQW distribution in the final PNPL solution. This is the first report in which the distribution of colloidal PNPLs is reliably controlled, and it enables us to report LSC devices based on PNPLs-poly(methyl methacrylate) (PMMA) composites having an optical conversion efficiency of 2.0%, which was reached on 10 × 10 cm panels. This is a 1.3-fold enhancement compared to the best previously reported room-temperature-fabricated perovskite LSCs.

RESULTS AND DISCUSSION

Solvent-Pb^{2+} Coordination Engineering and Synthesis of PNPLs

In a traditional room-temperature colloidal synthesis,[33] perovskite precursor salts are first dissolved in high-polarity solvents (e.g., dimethylformamide [DMF] and dimethyl sulfoxide [DMSO]), and this mixture is then added to an anti-solvent with lower polarity (e.g., chlorobenzene [CB], toluene): the rapid change in solubility forces precipitation of the constituent precursor salts, forming nanocrystals directly.

This method has been used to synthesize bromine-based PNPLs;[19] however, when we first applied this method to iodine-based PNPLs, we obtained weak emission (photoluminescence quantum yield [PLQY] < 0.1%) from the final products. We noticed that in the absorption spectrum of the precursor solution, there was a strong peak at 324 nm (Figure 1A): this peak can be attributed to solvated PbI_2 complexes in the precursor solution.[27] The weaker peak at 374 nm is attributed to PbI_3^-.[27] We noted that similar peaks were not present in the bromine-based precursor solution and hypothesized that the formation of iodoplumbate complexes—in particular PbI_2—was limiting the emissivity of the final iodine-based PNPLs. We reasoned that, because the PbI_2 complex is the farthest from the nominal [PbI_6] necessary to form the final perovskite and is the least reactive, its presence was preventing the formation of nanocrystals. We attribute the absence of bromoplumbate complexes to the stronger ionic attraction between Pb^{2+} and bromide in $PbBr_2$, as the bromide ion has smaller ionic radius than the iodide ion.
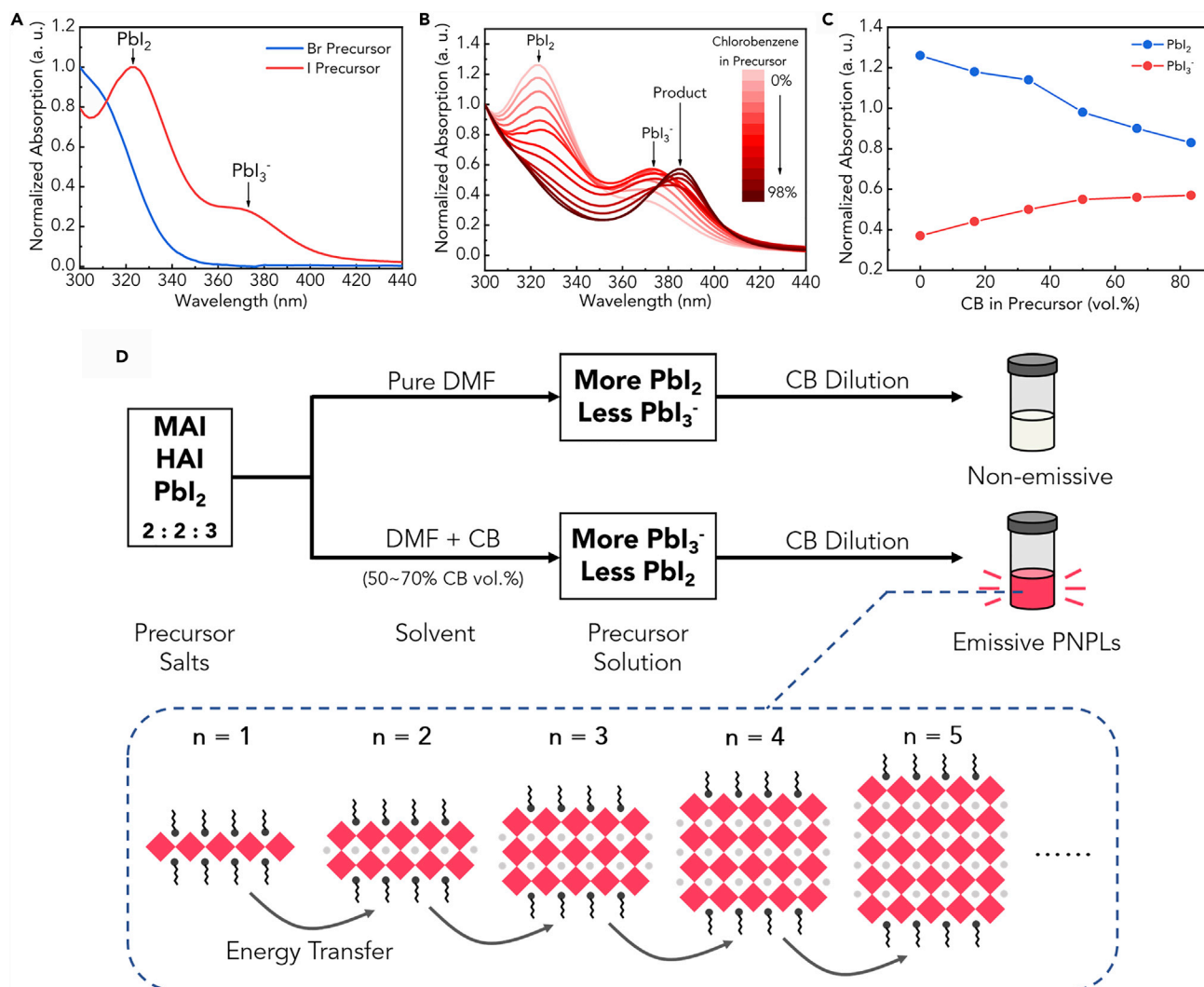
[1]Department of Electrical and Computer Engineering, University of Toronto, 10 King's College Road, Toronto, ON M5S 3G4, Canada

[2]Division of Physical Sciences and Engineering, King Abdullah University of Science and Technology (KAUST), Thuwal 23955-6900, Kingdom of Saudi Arabia

[3]Present address: Departments of Chemistry and Electrical & Computer Engineering, Centre for Advanced Materials and Related Technologies (CAMTEC), University of Victoria, 3800 Finnerty Rd, Victoria, BC V8P 5C2, Canada

[4]Lead Contact

*Correspondence: ted.sargent@utoronto.ca

https://doi.org/10.1016/j.joule.2020.01.003

Joule

CellPress

Figure 1. Solvent-Solute Coordination Engineering of PNPL Precursor Solutions

(A) Absorption spectra of 5 mM nominal n = 3 iodine- and bromine-based perovskite (HA$_2$MA$_2$Pb$_3$X$_{10}$, X = Br, I) precursors in pure DMF.

(B) Absorption spectra of 5 mM nominal n = 3 iodine-based perovskite HA$_2$MA$_2$Pb$_3$I$_{10}$ precursors in DMF-CB complex solvent with various CB percentages. Lines from light to dark red color denotes DMF/CB ratio of 1:0, 5:1, 2:1, 1:1, 1:2, 1:5, 1:10, 1:15, 1:20, 1:30, 1:40, and 1:50, respectively.

(C) Normalized absorption peak intensity of PbI$_2$ and PbI$_3^-$ as a function of CB percentage in precursor solution.

(D) Schematic illustration of the modified room-temperature colloidal synthesis of PNPLs through solvent-solute coordination engineering and schematic structure of reduced-dimensional PNPLs with different n values.

We sought therefore to modify the PbI$_2$ complex concentration in the precursor solution. As previously reported, the iodoplumbate distribution in the precursor solution is affected by several factors, including the Pb^{2+}/I$^-$ ratio,[27,29,31] solvent polarity,[28] and Lewis basicity[34] of the solution. We varied the Pb^{2+}/I$^-$ ratio (i.e., varying the nominal <n> value) while using DMF as precursor solvent, but the PbI$_2$ complex was still prominent in the precursor solution, and the final PNPLs were still unstable and weakly emitting. We then attempted to modify the solvent polarity and basicity, through the simple expedient of introducing CB, which was used later as the anti-solvent for the formation of the nanocrystals, into the precursor solution (see Experimental Procedures). We immediately noticed that the addition of CB significantly impacted the iodoplumbate complexes in the precursor solution. Figure 1B shows the variation in the absorption spectra of the precursor solution upon
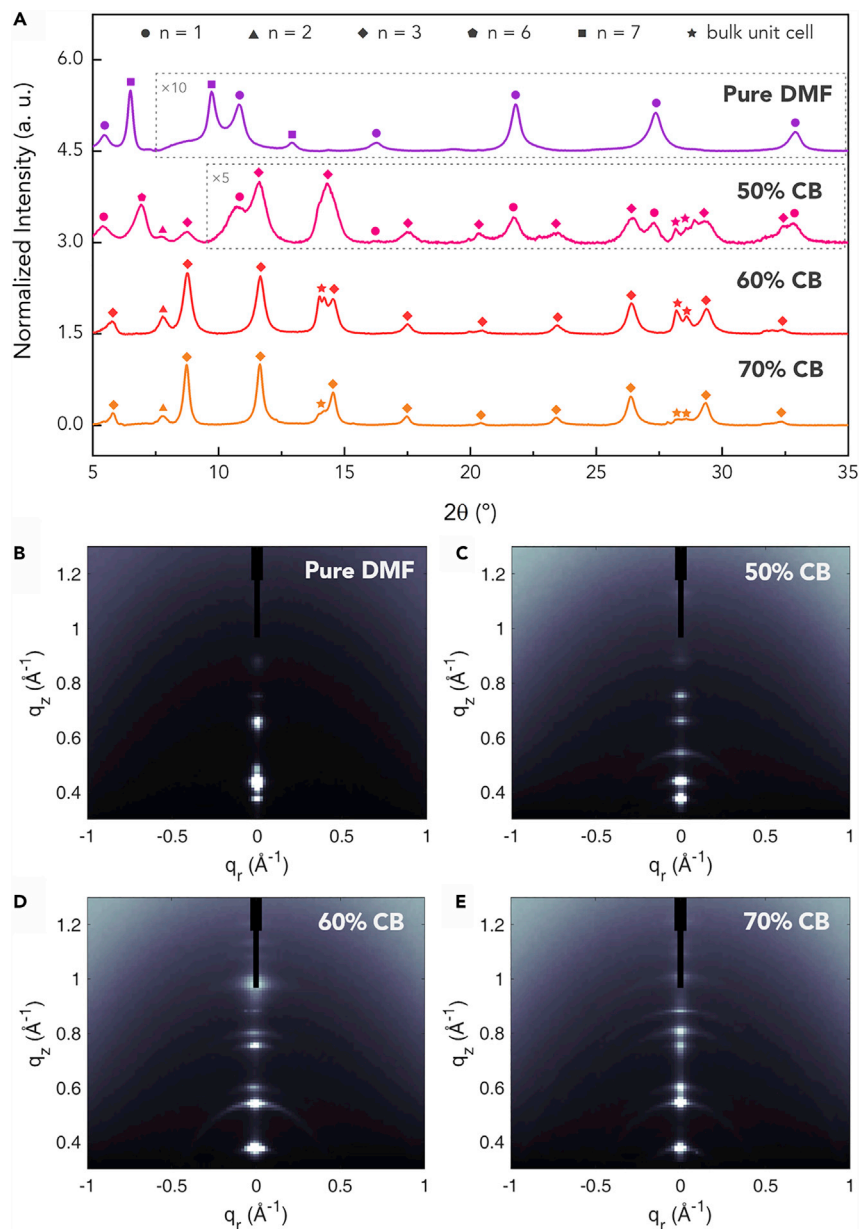
increasing the ratio of CB:DMF in the final solution. To avoid saturation of the optical density, the solution was diluted 50 times prior to the measurement. After dilution, the concentration of hexylammonium iodide (HAI), methylammonium iodide (MAI), and lead iodide (PbI_2) are 10, 10, and 15 mM, respectively. The absorption peaks at 324 and 374 nm correspond to PbI_2 and PbI_3^- complexes, respectively.[27]

To explore how CB percentage would affect the iodoplumbate distribution, we normalized the absorption at 300 nm for better comparison of the relative intensity of PbI_2 and PbI_3^- peaks. The concentration of PbI_3^- complex (the peak at 374 nm) continuously increases and the concentration of PbI_2 complex (the peak at 324 nm) decreases with increasing CB content, and when too much CB is added, the precursors salts are no longer stable. This results in a peak at 388 nm, which corresponds to perovskite product (Figure 1C), as the precursors begin to precipitate. The effect of CB percentage on the iodoplumbate distribution is also significant when the methylammonium (MA) is replaced with formamidinium (FA) (Figure S1). We attribute the variation in the iodoplumbate distribution to the polarity and Lewis basicity of solvent molecules, as has been previously reported.[28,34] DMF is a high-polarity solvent with a Gutmann's donor number (D_N) of 26.6 kcal/mol,[35,36] while CB is less polar with a D_N value of 3.3 kcal/mol.[35,36] D_N is a quantitative measure of Lewis basicity and describes the strength of interactions between Lewis-basic solvents and the Lewis-acidic Pb^{2+} center of iodoplumbate complexes in solution. DMF molecules with high D_N compete with I^- for coordination sites around Pb^{2+}, making PbI_2 complex dominant in the solution. The introduction of CB lowered the overall D_N of the precursor solution, promoting the formation of more reactive iodoplumbates with a higher number of coordinated iodine ions.

Structural Properties of PNPLs

To determine the effect of the iodoplumbate complexes on the MQW distribution of PNPLs, we studied the structural properties of drop-cast PNPL films prepared from different precursor solutions. It was not until the CB percentage in the precursor solution reached 50% (i.e., a 1:1 ratio of CB:DMF) that we obtained strongly emitting PNPLs (Figure 1D). When the CB percentage reached 80%, the precursor solution turned cloudy, indicating that PNPLs had already formed, even before being added to the larger amount of CB. The cloudy solution was non-emissive.

We thus focused our attention on drop-cast PNPL films with precursor CB percentages of 0%, 50%, 60%, and 70%, respectively to understand the impact the tailored iodoplumbate complex distribution had on the final PNPLs; we employed X-ray diffraction (XRD) and grazing incidence wide-angle X-ray scattering (GIWAXS) to study the structural properties of the films. XRD of PNPL films (Figure 2A) showed periodic (00l) diffraction peaks at low angles, indicating the nanoplatelets stacked parallel to the substrate. Although the perovskite precursor concentration and ratio (nominal <n> = 3) were fixed, each sample had a different MQW distribution— different sets of (00l) peaks of various n appeared with different relative intensities. The control film (0% CB) consisted mainly of n = 1 and n = 7 phases, while the film with 70% CB in precursor was predominantly composed of the n = 3 phase and a small amount of the n = 2 phase. The 60% CB film had a similar MQW distribution as the 70% one but had stronger bulk unit cell peak intensities at 14°, 14.2°, 28.2°, and 28.6°, indicating a higher portion of high n (>10) or bulk perovskite. In the 50% sample, n = 1, 2, 3, and 6 and bulk unit cell peaks all appeared, indicating that a broad MQW distribution was obtained; this provides both an improved absorption range and more efficient energy funneling, enabling a higher PLQY and optical conversion efficiency. GIWAXS measurements of the PNPL films yielded similar

Joule

Figure 2. Structural Studies of Drop-Cast PNPL Films

(A) X-ray diffraction of PNPL films.

(B–E) GIWAXS spectra of PNPL films with precursor CB percentage of 0% (B), 50% (C), 60% (D), and 70% (E).

peak information as shown in the XRD, while the integrated intensities of the (00*l*) peaks along the q_z direction indicated that these planes lay parallel to the substrate (Figures 2B–2E).

A different distribution of iodoplumbate species in the precursor solution resulted in different crystal formation kinetics of MQWs, affecting their final distribution. We probed *in situ* the formation of the nanoplatelets by measuring the PL spectra evolution during the reaction (Figure S2). PbI_3^- is closer than PbI_2 to the $[PbI_6]$

Joule

CellPress

octahedra framework in the final perovskite, as the Pb^{2+} has a higher coordination number with I^-. When a pure DMF is used as the precursor solvent, the high D_N value prevents the formation of higher-order iodoplumbate complexes: as a result, 2D perovskite with n = 1 (evidenced by the weak PL peak at ~520 nm), distinct from the nominal n = 3 precursor ratio, rapidly forms. The rapid formation of pure 2D perovskite is expected as n = 1 has the lowest formation energy and the strongest van der Waals interaction[25,37,38] between the stacked bulky organic cations (HA). After the consumption of most of the bulky organic cations, the remaining precursor salts were left to nucleate without the confining bulky cations, resulting in a large concentration of high n quantum wells. However, the emission of the solution rapidly (~2–3 s) decayed as the reaction progressed due to the unbalanced MQW distribution and the instability of the nanoplatelets in solution (Figures S2A and S2B). In contrast, when a high CB percentage (70%) is present in the precursor solution, there is an abundance of higher-order iodoplumbate complexes, which enables fast crystallization (in < 0.2 s) of PNPLs that are sharply distributed around the nominal starting ratio of n = 3 (Figures S2C and S2D). When an optimal ratio of CB is used, formation of both low n and higher n quantum wells occur; the low n quantum wells form faster due to lower formation energy.[25,37,38] As a result, the PL peak continuously red shifts during the first 10 s of the reaction. The final product has a uniform, broad distribution of quantum wells with efficient energy funneling (Figures S2E and S2F). We characterized the morphology of the as-synthesized nanoplatelets with transmission electron microscope (TEM): the PNPLs have a lateral size of ~20 nm and thicknesses ranging from 3–5 nm (Figure S3). The varied widths of the observed nanoplatelets confirm the PNPLs are composed of MQWs with different n values.
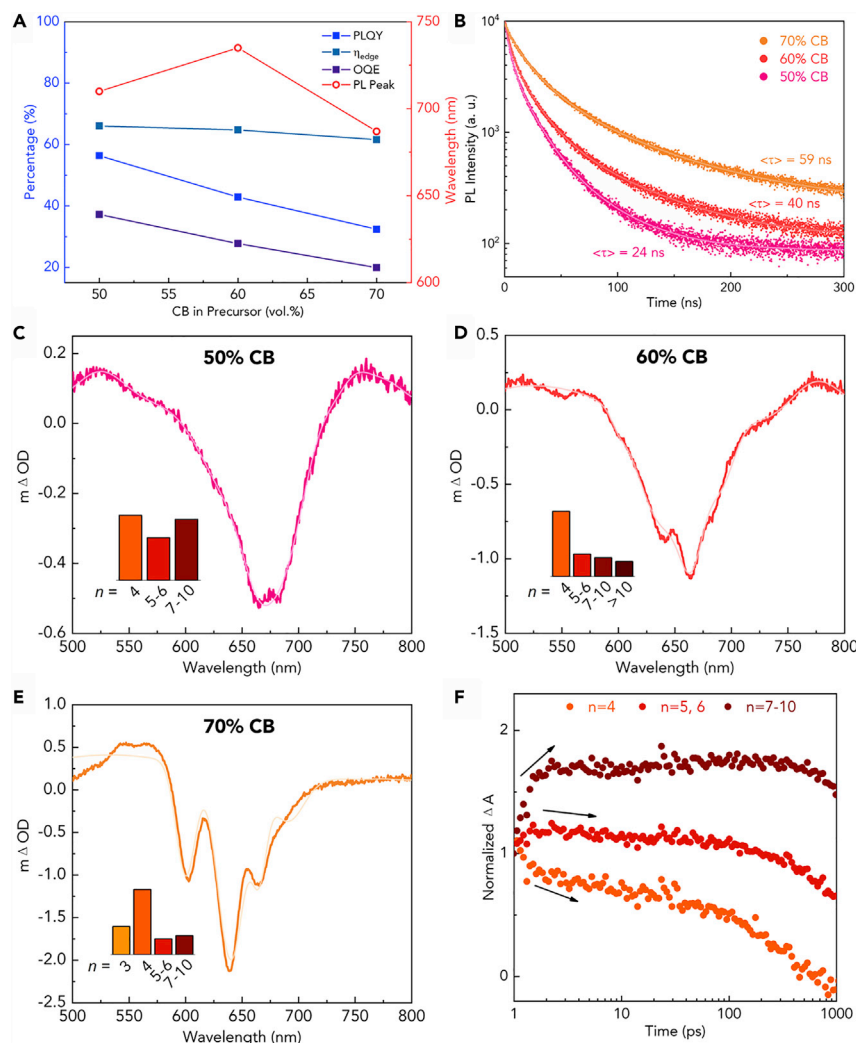
Photophysical Studies

We then diluted the PNPLs in a polymer host matrix of PMMA and drop-cast PNPLs-PMMA composites on a 2.5 × 2.5 cm glass slab to fabricate small-area LSCs and characterized their photophysical properties. To evaluate the optical loss, we measured the PLQY of the LSC devices before ($PLQY_{total}$) and after ($PLQY_{surface}$) covering the edges with opaque carbon paste. We then calculated the edge coupling efficiency η_{edge} using the following formula:

$$\eta_{edge} = \frac{PLQY_{total} - PLQY_{surface}}{PLQY_{total}}$$

The LSC device fabricated with 50% CB inclusion in the precursor solution has 56% PLQY with 65% edge coupling efficiency and a 37% OQE with the peak PL wavelength at 710 nm. The $PLQY_{total}$, OQE, and η_{edge} decrease when the CB percentage in precursor is increased to values greater than 50% (Figure 3A). We attribute the decreased efficiency to a decrease in radiative recombination, combined with larger absorption-photoluminescence spectral overlap (reduced Stokes shift) due to the sharp quantum well distribution around n = 3. Time-resolved photoluminescence (TRPL) spectra taken at the peak PL wavelength for each sample revealed that the average lifetime increased with increasing CB content (Figure 3B). Each PNPL should exhibit similar radiative rates, but the non-radiative rate will vary due to surface traps and proximity of neighboring PNPLs. We calculate the radiative lifetime τ_{rad} for each sample, given by

$$\tau_{rad} = \frac{\sum_{i=1}^{n} A_i \tau_i}{PLQY}$$

where τ_i is the single exciton decay lifetime and A_i is its relative fraction.[39] As shown in Table S1, τ_{rad} increases with CB percentage, indicating a decreased

Figure 3. Photophysical Studies of LSCs Based on PNPLs-PMMA Composites

(A) PL peak wavelength, PLQY, OQE, and edge coupling efficiency (η_{edge}) as a function of CB percentage in precursor solution.

(B) PL decay (discrete points) and its tri-exponential fit (solid line).

(C–E) TA spectra (solid line) of LSCs with precursor CB percentage of 50% (C), 60% (D), and 70% (E). Gaussian fitting of the TA spectra for various n values (dashed line) enable the identification of the distribution of bleach intensities (histograms [C]–[E]).

(F) TA spectra for 50% CB sample at various TA bleach peaks as a function of delay time.

radiative rate. The decreased radiative rate may be due to the decreased content of n = 7–10 nanoplatelets, which are excellent emitters when in a funneling structure;[25] as the radiative rate is extracted from the ensemble of different MQWs, it will be greatly influenced by the distribution of MQWs. Figure S4 shows the spectral overlap of the 50% CB sample compared to the 60% and 70% CB samples. To compare quantitatively the spectral overlap, we define the LSC quality factor Q_{LSC} as the ratio of the absorbance at 500 nm and the absorbance at the PL peak wavelength. As shown in Figure S5, the 50% CB sample has the highest Q_{LSC} of 34, corresponding to the lowest spectral overlap.

We also carried out narrowband ultrafast TA studies to probe the quantum well distribution and the charge transfer in each sample. Figures 3C–3E show the TA spectra

of each of the 50%, 60%, and 70% samples at a probe delay of 1 ps. In each case, a sum of Gaussian curves was used to fit the experimental curve.[40] We centered the Gaussian curves at the center absorption wavelength of different quantum wells.[40] By integrating the area of each curve, we estimate the distribution of quantum wells in each sample. For the 50% sample, a uniform distribution of n = 4–10 is observed. For the 60% sample, we observe a strong presence of n = 4, with the presence of some higher n peaks, up to bulk. For the 70% sample, there is predominantly n = 3 and n = 4. These distributions agree with the XRD obtained earlier, although these films were prepared with PMMA, whereas the XRD films were not.

Figure 3F shows the time evolution of various bleach peaks for the 50% sample (see also Figure S7 for the 60% and 70% samples). The data were normalized to the signal at 1 ps and offset for clarity. Over the first 100 ps, there is a significant rise in the bleach peak corresponding to the n = 7–10 signal, accompanied by a significant fall in the n = 3 sample. The n = 5–6 signal remains roughly constant over this time frame, indicating that there is transfer from the n = 3 to the n = 5–6 and n = 7–10, and also transfer from the n = 5–6 to the n = 7–10 wells. Photo-luminescence excitation (PLE) spectra (Figure S6) also evidence efficient energy transfer. Efficient energy transfer indicates that different n phases co-exist and interact within a given platelet, including when the PNPLs are incorporated into the PMMA matrix.[19]
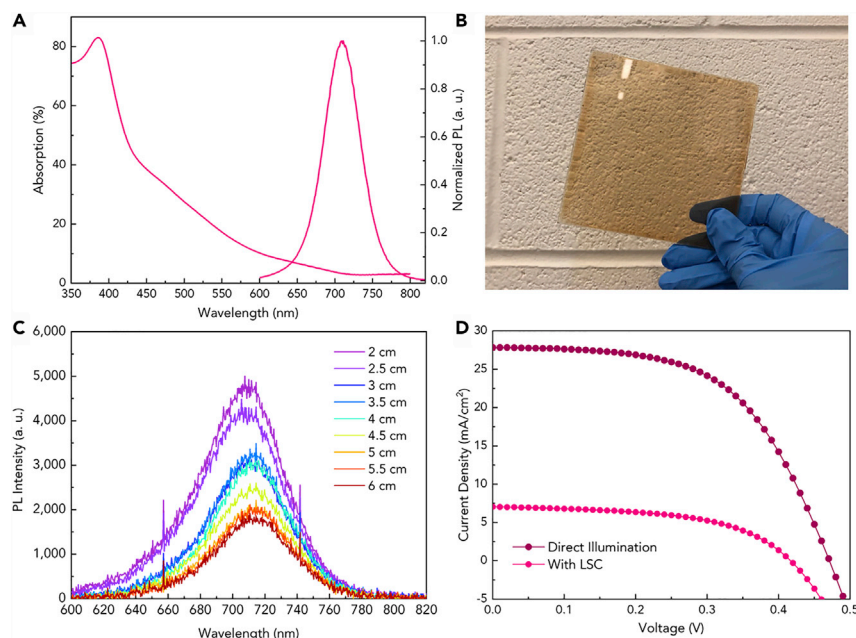
Performance of PNPLs in Large-Area LSCs

We fabricated large-area LSCs (10 × 10 × 0.2 cm) and acquired current density-voltage measurements for LSC devices under outdoor conditions to demonstrate application (Figures 4D and S8). PNPLs-PMMA composites were deposited on both sides of the glass substrate to maximize absorption while maintaining low reabsorption loss. We measured the photogenerated currents of a polycrystalline silicon (c-Si) solar cell with and without coupling to the edge of an LSC device. The optical conversion efficiency η_{opt} was calculated as:

$$\eta_{opt} = \frac{P_{out}}{P_{in}} = \frac{I_{LSC}}{I_{SC} \times G}$$

where I_{LSC} is the short circuit current generated by the c-Si solar cell coupled to the LSC, I_{SC} is the short circuit current of the same solar cell under direct solar illumination, and G is the geometric factor of the LSC film (G = Area$_{front}$/Area$_{edges}$). With an I_{LSC}/I_{SC} value of 25.3% and a geometric factor of 12.5, the best LSCs, with precursor CB percentage of 50%, achieved an optical conversion efficiency of 2.0% (Figure 4D). This is a 1.34× improvement compared to the previously reported 10 × 10 × 0.2 cm LSCs based on the best perovskite LSC fabricated at room temperature. The external OQE, which is defined as the ratio of the number of photons emitted from the edges of the LSC to the total incident photons, is 1.1% (Note S1). This also yields a 1.26× improvement compared to the LSCs based on bromine-based PNPLs. LSCs with 60% and 70% precursor CB percentage have η_{opt} of 1.7% and 1.3%, respectively (Figures S8B and S8C). In addition to the improved performance, our LSCs have a neutral color (Figure 4B) compared to the green color of the bromine-based LSCs.[19] The neutral color is compatible with integration of LSCs.

We further characterized the best performing LSCs made from the 50% CB PNPLs. As seen in Figure 4A, due to the large Stokes shift introduced by the MQW distribution, the spectral overlap between the absorsion and emission spectra is significantly suppressed. We confirmed the suppressed reabsorption by measuring the PL spectra from the waveguide as a function of optical path by varying the

Joule

Figure 4. Solvent-Solute Coordination Engineering Enables Low-Loss Large-Area Perovskite LSCs

(A) Absorption and photoluminescence spectra of LSCs of perovskite NPLs.

(B) Photograph of a 10 × 10 cm PNPL-based LSC.

(C) Photoluminescence spectra of PNPLs collected at the LSC edge as a function of the distance between the excitation spot and the collection edge.

(D) The J-V curves of the c-Si solar cell with and without coupling to the edges of the PNPL-based LSC.

excitation-collection distance. The peak PL intensity retained 40% of its initial value at 6 cm optical length when compared with the 2 cm optical length (Figure 4C). We also characterized the morphology and roughness of the LSC surface using atomic force microscopy (AFM). As shown in Figure S9, the PNPLs-PMMA surface has a root mean square (RMS) roughness of 0.6 nm. Scattering loss is suppressed by the smooth surface. In light of the high optical efficiency, scattering loss within the PNPLs-PMMA composite is low, and we propose that the PNPLs are substantially evenly distributed in the PMMA matrix.

Conclusions

In summary, we demonstrate that solvent coordination with Pb^{2+} in iodine-based perovskite precursor solution can be engineered by varying the average polarity and Lewis basicity of the precursor solvent, and this greatly impacts the crystallization kinetics of PNPL formation and the subsequent final MQW distribution. We determined that a 50% CB + 50% DMF combination of precursor solvent tunes the crystallization kinetics such that a uniform MQW distribution is obtained, which improves both energetic funneling and minimizes reabsorption loss. Only with this method can we obtain highly emissive iodine-based colloidal PNPLs with broad and even MQW distribution—the PLQY of the PNPLs achieved 56% in film. The 10 × 10 cm LSC panel based on the corresponding PNPLs-PMMA composites achieved an optical conversion efficiency of 2.0%, which is the highest among room-temperature-fabricated perovskite LSCs. This work offers improved syntheses of iodine-based nanocrystals, enabling their application in broader optoelectronic devices.

Joule

EXPERIMENTAL PROCEDURES

Materials

Lead bromide ($PbBr_2$, 99.9%) and lead iodide (PbI_2, 99.9%) were purchased from Alpha Aesar. N,N-dimethylformamide (DMF, 99.8%), CB (99.8%), oleic acid (>99%), oleylamine (>98%), and PMMA (molecular weight $\sim$120,000 by gel permeation chromatography) were purchased from Sigma-Aldrich. Methylammonium bromide (MABr), MAI, hexylammonium bromide (HABr), and HAI were purchased from Great Cell Solar. All chemicals were used as procured without further purification.

Perovskite Nanoplatelet Synthesis

0.2 M HAI, 0.2 M MAI, and 0.3 M PbI_2 were dissolved in DMF or DMF-CB complex solvent. The HAI:MAI:PbI_2 = 2:2:3 ratio correspond to a nominal <n> = 3 reduced-dimensional perovskite composition $(HA)_2(MA)_{n-1}Pb_nI_{3n+1}$. 5 µL of oleylammine and 10 µL of oleic acid was then added in 0.4 mL of the solution. 40 µL of stock precursor solution was then quickly added to 1 mL of CB under vigorous stirring to immediately form PNPLs. The as-prepared PNPL solution was then filtered by the 0.22 µm PTFE filter. 1 mL of the final solution was then mixed with 1 mL PMMA solution (300 mg/mL in CB) to form the PNPLs-PMMA composites for LSC fabrication. PNPL films without PMMA were fabricated by drop-casting the filtered PNPL solution on the glass substrate directly and dried under vacuum for 20 min.

Absorption Measurements

Optical absorption spectra were measured with a Perkin Elmer 950 UV-vis-NIR spectrometer equipped with an integrating sphere for thin-film measurements.

X-Ray Diffraction Measurements

X-ray diffractograms were recorded using a Rigaku MiniFlex 600 powder X-ray diffractometer equipped with a NaI scintillation counter and using monochromatized Cu Kα radiation (λ = 1.5406 Å), with a detector angle (2θ) step of 0.02°.

GIWAXS Measurements

GIWAXS measurements were conducted at the Hard X-ray MicroAnalysis (HXMA) beamline of the Canadian Light Source (CLS). An energy of 17.998 keV (λ = 0.6888 Å) was selected using a Si(111) monochromator. Patterns were collected on a SX165 CCD camera (Rayonix) placed at a distance of 155 mm from the sample. A lead beamstop was used to block the direct beam. Images were calibrated using LaB_6 and processed via the Nika[41] software package and the GIXSGUI[42] MATLAB plugin.

TEM Measurements

TEM analysis was carried out with a Titan TEM (FEI Company) operating at a beam energy of 300 keV and equipped with a Tridiem post-column energy filter (Gatan, Inc.).

AFM Measurements

AFM measurements were done with an Asylum Research Cypher operating in tapping mode with an AC240TM-R3 probe. The collected data were processed via the WSxM software.[43]

Transient Absorption Measurements

Femtosecond laser pulses of a 1,030 nm fundamental beam at a 5 kHz repetition rate were produced using a regenerative amplified Yb:KGW laser (PHAROS, Light

Conversion). Part of the fundamental beam was used to pump an optical parametric amplifier (ORPHEUS, Light Conversion) to serve as a narrowband pump, while the other part was focused into a sapphire crystal to generate a white-light supercontinuum probe (400–1,000 nm window with various optical filters). Both the pump and probe pulses were directed into a commercial TA spectrometer (Helios, Ultrafast). Delaying the probe pulse relative to the pump provides a time window of up to 8 ns, and the time resolution of these experiments was ∼300 fs (estimated by the rise time of signal amplitudes in TA spectra).

Fabrication of LSCs
For large-area device, 4 mL of PNPLs-PMMA composites was poured onto a glass substrate (10 × 10 cm). To form a uniform solution film, a glass rod was swiftly translated over the substrate. The film was then dried under vacuum for 2 h to make all the solvent fully evaporated. For small-area device (2.5 × 2.5 cm), composites were drop-casted on the substrate directly and dried under vacuum for 20 min.

In Situ Photoluminescence Measurements
During the formation of PNPLs in solution, the emitted light is collected and focused through a lens and connected to a visible spectrophotometer (Ocean Optics USB 2000) using an optical fiber. The integration time is 50 ms for the 0% CB samples and 10 ms for the 50% and 70% CB samples, respectively. A 375 nm ultraviolet light emitting diode was used as the excitation source.

Photoluminescence Measurements
PL spectra for PNPLs-PMMA composite films were recorded using a Horiba Fluorolog system equipped with a single grating and a time-correlated single-photon counting detector. For steady-state PL measurements, the excitation source is a monochromated Xe lamp. For time-resolved PL, we used a 504 nm laser diode with the overall time resolution of $\Delta t \sim 0.11$ ns. PLQY measurements were implemented by coupling a Quanta-Phi integrating sphere to the Flurolog system with optical fiber bundles. For all PLQY measurements, the Fluorolog was set to an excitation wavelength at 500 nm with a 5 nm bandpass for both the excitation and emission slits to ensure high signal-to noise ratios. OQE was obtained by subtracting PLQY of the film with clear edges from that of the film with edges blocked by black carbon paint.

J-V Measurements on Perovskite LSCs
Polycrystalline silicon (c-Si) solar cells (500 mA/0.5 V, Solar Made) with an area of 2.5 × 5 cm were used for LSC characterization. The PV cell was attached to one edge of an LSC with black tape covering the area of the cell exposed outside of the LSC edge. To measure the current density-voltage (J-V) characteristics of c-Si solar cells and the LSC-PV system, a Keithley 2400 sourcemeter was used under outdoor conditions on a sunny day. The LSC film was perpendicular to the direct beam component of irradiance.

SUPPLEMENTAL INFORMATION
Supplemental Information can be found online at https://doi.org/10.1016/j.joule.2020.01.003.

Joule

CellPress

AUTHOR CONTRIBUTIONS

Z.L., A.J., M.W., M.I.S., and E.H.S. conceived the idea and proposed the experimental design. Z.L. synthesized the materials and fabricated the devices. Z.L., J.M.P., and Y.L. performed the optical measurements. A.J. conducted the TA measurements. A.J. was responsible for the GIWAXS measurements. X.Z., J.L., and O.M.B. conducted the TEM measurements. Z.L., A.J., and E.H.S. co-wrote the manuscript. All authors contributed in data analysis and read and commented on the manuscript.

DECLARATION OF INTERESTS

The authors declare no competing interests.

REFERENCES

1. Meinardi, F., Colombo, A., Velizhanin, K.A., Simonutti, R., Lorenzon, M., Beverina, L., Viswanatha, R., Klimov, V.I., and Brovelli, S. (2014). Large-area luminescent solar concentrators based on 'stokes-shift-engineered' nanocrystals in a mass-polymerized PMMA matrix. Nat. Photonics 8, 392–399.

2. Meinardi, F., McDaniel, H., Carulli, F., Colombo, A., Velizhanin, K.A., Makarov, N.S., Simonutti, R., Klimov, V.I., and Brovelli, S. (2015). Highly efficient large-area colourless luminescent solar concentrators using heavy-metal-free colloidal quantum dots. Nat. Nanotechnol. 10, 878–885.

3. Zhou, Y., Benetti, D., Fan, Z., Zhao, H., Ma, D., Govorov, A.O., Vomiero, A., and Rosei, F. (2016). Near infrared, highly efficient luminescent solar concentrators. Adv. Energy Mater. 6, 1501913.

4. Li, H., Wu, K., Lim, J., Song, H.-J., and Klimov, V.I. (2016). Doctor-blade deposition of quantum dots onto standard window glass for low-loss large-area luminescent solar concentrators. Nat. Energy 1, 16157.

5. Zhao, H., Benetti, D., Jin, L., Zhou, Y., Rosei, F., and Vomiero, A. (2016). Absorption enhancement in "giant" core/alloyed-shell quantum dots for luminescent solar concentrator. Small 12, 5354–5365.

6. Meinardi, F., Ehrenberg, S., Dhamo, L., Carulli, F., Mauri, M., Bruni, F., Simonutti, R., Kortshagen, U., and Brovelli, S. (2017). Highly efficient luminescent solar concentrators based on earth-abundant indirect-bandgap silicon quantum dots. Nat. Photonics 11, 177–185.

7. Bergren, M.R., Makarov, N.S., Ramasamy, K., Jackson, A., Guglielmetti, R., and McDaniel, H. (2018). High-performance CuInS2 quantum dot laminated glass luminescent solar concentrators for Windows. ACS Energy Lett. 3, 520–525.

8. Brennan, L.J., Purcell-Milton, F., McKenna, B., Watson, T.M., Gun'ko, Y.K., and Evans, R.C. (2018). Large area quantum dot luminescent solar concentrators for use with dye-sensitised solar cells. J. Mater. Chem. A 6, 2671–2680.

9. Debije, M.G., and Verbunt, P.P.C. (2012). Thirty years of luminescent solar concentrator research: solar energy for the built environment. Adv. Energy Mater. 2, 12–35.

10. Batchelder, J.S., Zewail, A.H., and Cole, T. (1981). Luminescent solar concentrators. 2: experimental and theoretical analysis of their possible efficiencies. Appl. Opt. 20, 3733–3754.

11. Kinderman, R., Slooff, L.H., Burgers, A.R., Bakker, N.J., Büchtemann, A., Danz, R., and van Roosmalen, J.A.M. (2007). I-V performance and stability study of dyes for luminescent plate concentrators. J. Sol. Energy Eng. 129, 277–282.

12. Baumberg, I., Berezin, O., Drabkin, A., Gorelik, B., Kogan, L., Voskobojnik, M., and Zaidman, M. (2001). Effect of polymer matrix on photo-stability of photo-luminescent dyes in multi-layer polymeric structures. Polymer Degrad. Stabil. 73, 403–410.

13. Mansour, A.F., Killa, H.M.A., El-Wanees, S.A., and El-Sayed, M.Y. (2005). Laser dyes doped with poly (ST-Co-MMA) as fluorescent solar collectors and their field performance. Polym. Test 24, 519–525.

14. Moudam, O., Rowan, B.C., Alamiry, M., Richardson, P., Richards, B.S., Jones, A.C., and Robertson, N. (2009). Europium complexes with high total photoluminescence quantum yields in solution and in PMMA. Chem. Commun. (Camb.), 6649–6651.

15. Reisfeld, R., and Neuman, S. (1978). Planar solar energy converter and concentrator based on uranyl-doped glass. Nature 274, 144–145.

16. Reisfeld, R., and Kalisky, Y. (1981). Nd3+ and Yb3+ germanate and tellurite glasses for

Joule

CellPress

fluorescent solar energy collectors. Chem. Phys. Lett. *80*, 178–183.

17. Reisfeld, R. (1983). Future technological applications of rare-earth-doped materials. J. Less Common Met *93*, 243–251.

18. Tong, J., Luo, J., Shi, L., Wu, J., Xu, L., Song, J., Wang, P., Li, H., and Deng, Z. (2019). Fabrication of highly emissive and highly stable perovskite nanocrystal-polymer slabs for luminescent solar concentrators. J. Mater. Chem. A *7*, 4872–4880.

19. Wei, M., de Arquer, F.P.G., Walters, G., Yang, Z., Quan, L.N., Kim, Y., Sabatini, R., Quintero-Bermudez, R., Gao, L., Fan, J.Z., et al. (2019). Ultrafast narrowband exciton routing within layered perovskite nanoplatelets enables low-loss luminescent solar concentrators. Nat. Energy *4*, 197–205.

20. Mendewala, B., Nikolaidou, K., Hoffman, C., Sarang, S., Lu, J., Ilan, B., and Ghosh, S. (2019). The potential of scalability in high efficiency hybrid perovskite thin film luminescent solar concentrators. Sol. Energy *183*, 392–397.

21. Meinardi, F., Akkerman, Q.A., Bruni, F., Park, S., Mauri, M., Dang, Z., Manna, L., and Brovelli, S. (2017). Doped halide perovskite nanocrystals for reabsorption-free luminescent solar concentrators. ACS Energy Lett. *2*, 2368–2377.

22. Bagherzadeh-Khajehmarjan, E., Nikniazi, A., Olyaeefar, B., Ahmadi-Kandjani, S., and Nunzi, J.-M. (2019). Bulk luminescent solar concentrators based on organic-inorganic $CH_3NH_3PbBr_3$ perovskite fluorophores. Sol. Energ. Mater. Sol. Cell. *192*, 44–51.

23. Zhao, H., Zhou, Y., Benetti, D., Ma, D., and Rosei, F. (2017). Perovskite quantum dots integrated in large-area luminescent solar concentrators. Nano Energy *37*, 214–223.

24. Zhao, H., Sun, R., Wang, Z., Fu, K., Hu, X., and Zhang, Y. (2019). Zero-dimensional perovskite nanocrystals for efficient luminescent solar concentrators. Adv. Funct. Mater. *29*, 1902262.

25. Yuan, M., Quan, L.N., Comin, R., Walters, G., Sabatini, R., Voznyy, O., Hoogland, S., Zhao, Y., Beauregard, E.M., Kanjanaboos, P., et al.

(2016). Perovskite energy funnels for efficient light-emitting diodes. Nat. Nanotechnol. *11*, 872–877.

26. Oldenburg, K., Vogler, A., Mikó, I., and Horváth, O. (1996). Photoredox decomposition of tin (II), lead (II), antimony (III) and bismuth (III) iodide complexes in solution. Inorg. Chim. Acta *248*, 107–110.

27. Stamplecoskie, K.G., Manser, J.S., and Kamat, P.V. (2015). Dual nature of the excited state in organic–inorganic lead halide perovskites. Energy Environ. Sci. *8*, 208–215.

28. Rahimnejad, S., Kovalenko, A., Forés, S.M., Aranda, C., and Guerrero, A. (2016). Coordination chemistry dictates the structural defects in lead halide perovskites. ChemPhysChem *17*, 2795–2798.

29. Sharenko, A., Mackeen, C., Jewell, L., Bridges, F., and Toney, M.F. (2017). Evolution of Iodoplumbate complexes in methylammonium lead iodide perovskite precursor solutions. Chem. Mater. *29*, 1315–1320.

30. Shin, G.S., Kim, S.G., Zhang, Y., and Park, N.G. (2019). A correlation between Iodoplumbate and photovoltaic performance of perovskite solar cells observed by precursor solution aging. Small Methods, 1900398.

31. Radicchi, E., Mosconi, E., Elisei, F., Nunzi, F., and De Angelis, F. (2019). Understanding the solution chemistry of lead halide perovskites precursors. ACS Appl. Energy Mater. *2*, 3400–3409.

32. Pratap, S., Keller, E., and Müller-Buschbaum, P. (2019). Emergence of lead halide perovskite colloidal dispersions through aggregation and fragmentation: insights from the nanoscale to the mesoscale. Nanoscale *11*, 3495–3499.

33. Weidman, M.C., Seitz, M., Stranks, S.D., and Tisdale, W.A. (2016). Highly tunable colloidal perovskite nanoplatelets through variable cation, metal, and halide composition. ACS Nano *10*, 7830–7839.

34. Hamill, J.C., Schwartz, J., and Loo, Y.-L. (2018). Influence of solvent coordination on hybrid

organic–inorganic perovskite formation. ACS Energy Lett. *3*, 92–97.

35. Reichardt, C., and Welton, T. (2011). Solvents and Solvent Effects in Organic Chemistry (John Wiley & Sons).

36. Laurence, C., and Gal, J.-F. (2009). Lewis Basicity and Affinity Scales: Data and Measurement (John Wiley & Sons).

37. Quan, L.N., Zhao, Y., García de Arquer, F.P., Sabatini, R., Walters, G., Voznyy, O., Comin, R., Li, Y., Fan, J.Z., Tan, H., et al. (2017). Tailoring the energy landscape in Quasi-2D halide perovskites enables efficient green-light emission. Nano Lett. *17*, 3701–3709.

38. Xing, J., Zhao, Y., Askerka, M., Quan, L.N., Gong, X., Zhao, W., Zhao, J., Tan, H., Long, G., Gao, L., et al. (2018). Color-stable highly luminescent sky-blue perovskite light-emitting diodes. Nat. Commun. *9*, 3541.

39. Makarov, N.S., Guo, S., Isaienko, O., Liu, W., Robel, I., and Klimov, V.I. (2016). Spectral and dynamical properties of single excitons, biexcitons, and trions in cesium-lead-halide perovskite quantum dots. Nano Lett. *16*, 2349–2362.

40. Quintero-Bermudez, R., Gold-Parker, A., Proppe, A.H., Munir, R., Yang, Z., Kelley, S.O., Amassian, A., Toney, M.F., and Sargent, E.H. (2018). Compositional and orientational control in metal halide perovskites of reduced dimensionality. Nat. Mater. *17*, 900–907.

41. Ilavsky, J. (2012). Nika: software for two-dimensional data reduction. J. Appl. Crystallogr. *45*, 324–328.

42. Jiang, Z. (2015). GIXSGUI: a MATLAB toolbox for grazing-incidence X-ray scattering data visualization and reduction, and indexing of buried three-dimensional periodic nanostructured films. J. Appl. Crystallogr. *48*, 917–926.

43. Horcas, I., Fernández, R., Gómez-Rodríguez, J.M., Colchero, J., Gómez-Herrero, J., and Baro, A.M. (2007). WSXM: a software for scanning probe microscopy and a tool for nanotechnology. Rev. Sci. Instrum. *78*, 013705.